Refractive indices and extinction coefficients of p-type doped Germanium wafers for photovoltaic and thermophotovoltaic devices

E. Blanco[1], P. Martín[2], M. Domínguez[1], P. Fernández-Palacios[2], I. Lombardero[2,3], C. Sanchez-Perez[2], I. García[2], C. Algora[2], M. Gabás[2*]

[1] Departamento de Física de la Materia Condensada & IMEYMAT: Institute of Research on Electron Microscopy and Materials, University of Cadiz, E11510 Puerto Real, Cádiz, Spain

[2] Instituto de Energía Solar, Universidad Politécnica de Madrid, 28040 Madrid, Spain.

[3] MN8 Energy, 28224 Pozuelo de Alarcón, Madrid, Spain

* corresponding author, mercedes.gabas@upm.es

Keywords: Ge wafers, spectroscopic ellipsometry, complex refractive index, Ge solar cells, thermophotovoltaics, solar cell modelling

Abstract

Our work is primarily driven by the absence of optical parameters for p-type Ge wafers, adaptable to any specific doping value, and, at the same time, able to cover any application from infrared to ultraviolet regime. To address this, we have determined the complex refractive indices of p-type commercial Ge wafers through a wide spectral range (200-25000 nm) employing spectroscopic ellipsometry and transmittance measurements. The doping levels in these wafers vary between 10^{15} and 10^{18} cm^{-3}, which are most commonly used in photovoltaic, thermophotovoltaic and optoelectronic applications. Our data fitting procedure resulted in a dielectric function that successfully reproduces not only the critical points associated with interband transitions above the bandgap, but also absorption features below the bandgap connected to intraband processes. Consequently, we obtained the complex refraction indices of these Ge wafers as a function of dopant concentration, and these have been corroborated through experimental reflectance and transmittance measurements. Additionally, we achieved a successful validation of these refractive indices by simulating the external quantum efficiency of Ge single-junction solar cell with two different thickness fabricated on a Ge wafer with a different doping level than those analysed in this study.

1. INTRODUCTION

Ge wafers are the most widespread substrate used for commercial III-V multijunction solar cells (MJSC) [1], and they are gaining a prominent position in some other device markets like vertical cavity surface emitting lasers (VCSEL) [2]. Besides these applications in III-V compound devices, Ge substrates have extended their applications as physical support for a wide variety of thin films. For example, Ge wafers have recently demonstrated their possibilities as substrates for graphene which has been synthesized directly on p-type Ge substrates by chemical vapor deposition (CVD) [3,4], or ion implantation [5]. Epitaxial IV-VI chalcogenide structures [6], as well as Ge alloys [7,8], have also been grown on Ge substrates. Ge wafers have thus to fit high-quality requirements in order to guarantee their suitability in very different applications [9,10]. In the case of commercial Ge wafers, special attention must be paid to the differences among wafers from the same batch and/or supplier [11], and, besides, to the chemical state of the Ge wafer surface [12]. This last point may have a critical influence on the wafer optical properties since the wafer surface constitutes a different layer with its own optical response. Therefore, a systematic and thorough knowledge of the substrate characteristics seems necessary prior to the growth of any optoelectronic device onto these Ge wafers.

In particular, for its incorporation in MJSC, the knowledge of the Ge optical properties is a crucial step in the design and growth of optimized solar cells, since the Ge subcell has an active and important role in the final device performance, especially in the infrared (IR) part of the spectrum [13]. The study of Ge optical properties was the subject of several works during the past century. The first papers were focused on the IR range (from some meV up to 0.8 eV) and described absorption bands related to free-carrier density in doped Ge [14,15,16]. The studied range was extended up to 27eV in the work of Rustgi et al [17]. The heavily doped Ge spectrum between near-infrared (NIR) and near ultraviolet (UV) was thoroughly studied using spectroscopic ellipsometry in [18]. More recently, due to its potential exploitation in photonics, germanium optical properties and or/dielectric function have been the subject of several articles, both in the IR and the visible (Vis) range. IR range is widely explored in [19] for n- and p-type doped Ge, though the covered wavelength range starts at 2 microns where Ge subcells in MJSC do not operate. The proposed tendencies fit moderately with the experiments but some discrepancies with [16] are noticed. For wavelengths below 2.5 microns the Sopra database can be used [20]. The NIR-Vis-UV Ge dielectric function has been studied in several recent works, each one focused on a particular issue, the GeO_2 layer onto Ge wafer [21], n-type doped Ge [22], and the temperature dependence of the Ge dielectric function [23].

For MJSCs and other photovoltaic applications, p-type Ge substrates are preferred over n-type ones since the Ge subcell is typically formed by phosphorous or arsenic diffusion while Metal Organic Vapor Phase Epitaxy (MOVPE) growth of the top passivation layers of GaInP or GaAs, respectively. This approach is followed in the III-V MJSC [13] and also in the thermophotovoltaic devices [24]. The range of useful p-dopant concentrations for such applications typically covers from 10^{15} to 10^{18} cm^{-3}. The modelling and simulation of the optical performance of these devices cannot be reliably done with the existing literature data, either because most of the published works are from tens of years ago, so they are not referred to current commercial Ge wafers which

have experienced a significant quality improvement since then, or because they are referred to n-type germanium, or because optical parameters have not been validated against different experimental data. In any case, none of the existing works provides the complex refractive indices for p-type Ge covering the spectral range from 0.2 to 25 microns, which is mainly required for photovoltaic and thermophotovoltaic devices. Furthermore, there are no reliable data about free-carrier absorption in p-type germanium as a function of doping level, which is of paramount importance in upcoming applications looking for lightweight and flexibility by means of thinning the Ge substrate and also in the reduction of operation temperature of devices [25].

In this work, we aim to fully characterize the optical behavior of p-type commercial Ge wafers, covering an ample range of dopant concentrations (10^{15} – 10^{18} cm^{-3}) in the UV, visible and IR spectrum (from 0.2 to 25 microns). For such purpose, the refraction index and the extinction coefficient have been deduced from spectroscopic ellipsometry measurements in combination with spectrophotometry data, and the absorption coefficient has been calculated. The goodness of these data has been validated against experimental transmittance and reflectance measurements, showing the appropriateness of these refractive indices to explain the optical behavior of our Ge wafers. Moreover, the external quantum efficiency (EQE) of Ge single-junction solar cells fabricated on a commercial Ge substrate with a different p-type concentration than those of the wafers measured here, have been modelled using interpolated optical parameters from those obtained in this work, and compared with the experimental one for an additional validation. The Ge single-junction solar cells were fabricated on two different Ge substrate thickness, in order to further extend the validation of our results to thinned solar cells.

2. MATERIALS AND METHODS

2.1. Materials

For this study, we used four commercial Ge epi-wafer electronic grade types with an [100] orientation. Doping levels (p-type) ranged from 10^{15} (almost intrinsic) to 10^{18} cm^{-3}, with the aim of covering the most interesting values for current Ge devices. Nominal specifications provided by the manufacturer are gathered in Table 1.

Table 1: Nominal characteristics of the commercial Ge wafers analyzed in this work. Samples are sorted in decreasing order according to the nominal doping level from top to bottom. The same criterion will be used along this paper for tables and legends inside figures.

Sample	Dopant	Resistivity (Ω cm)	Doping concentration (cm^{-3})	Thickness (μm)	Diameter (mm)	Dislocation density (counts/cm^2)
77942	Ga	0.009-0.03	10^{18}	330-355	76.2-76.7	0.0000
77944	Ga	0.03-0.07	10^{17}	330-355	76.2-76.7	0.0000
77943	Ga	0.2-0.4	10^{16}	330-355	76.2-76.7	0.0000
96132	undoped	40	10^{15}	475-525	50.7-50.9	0.0000

2.2. Spectroscopic ellipsometry

UV-Visible-NIR spectroscopic ellipsometry (SE) measurements were used to acquire the ellipsometric angles Ψ and Δ, and the depolarization spectra, in the range 200-2500 nm with 5 nm steps (i.e., 6.2-0.5 eV with steps of 0.01 eV), on a J.A. Woollam VASE vertical variable-angle-of-incidence rotating-analyzer ellipsometer, with a computer-controlled Berek wave-plate retarder (Automatic Retarder). To reduce experimental errors, all data were obtained by averaging two-zone measurements with equal and opposite polarizer angles. Data were acquired at three angles of incidence (50°, 60°, and 70°). The time required to acquire data for each sample was several hours. Monochromatic light was produced by an HS-190 double monochromator, fitted with three sets of gratings for the NIR, Vis, and quartz-UV portions of the spectral range. We used a 75W Xe short-arc lamp (Hamamatsu L10873) to produce the incident monochromatic beam and a UV-Vis-NIR optical fiber, avoiding any opaque region in the studied spectral range.

Infrared Spectroscopy Ellipsometry (IRSE) measurements were carried out on a J.A. Woollam IR-VASE Mark II ellipsometer, which integrates a Fourier Transform Infrared (FTIR) interferometer source with a rotating compensator ellipsometer. During the measurement, the compensator was rotated 360° in a series of steps, and an intensity spectrum related to the sample optical properties was recorded at each step. The Ψ and Δ spectra for each sample were then determined from a combination of the intensity spectra from each compensator position. The photon energy range was 400-5000 cm^{-1} with a step size of 8 cm^{-1}, (i.e., 0.05-0.62 eV with steps of 0.01 eV), and the incident angles were 50°, 60° and 70°.

From the combination of both experiments, we obtained the characterization of the samples in a global range of 200-25000 nm. Modeling of experimental IRSE and SE data was performed using the WVASE (J.A. Woollam Co. Inc.) software package.

2.3. Hall effect measurements

To confirm the nominal resistivity values provided by the Ge wafer manufacturer in Table 1 and to obtain the necessary electronic parameters for fitting the optical model deduced from the ellipsometric measurements, Hall effect and sheet resistivity measurements were performed, at room temperature, with the Van der Pauw method using a Linseis HCS 1 system, equipped with a 12.5 mm × 12.5 mm sample board and a 0.7 T permanent magnet.

2.4. Transmittance and reflectance measurements

To further improve the results obtained during the modelling of the SE measurements, UV-Vis~~ible~~-NIR transmittance and reflectance were also measured on each Ge wafer. An Agilent Cary 7000 spectroradiometer equipped with an integrating sphere was used to measure both parameters within the 300-2500 nm range in 1 nm steps (i.e., 4.1-0.5 eV with steps of 0.01 eV). All the Ge wafers were measured at a normal incidence angle. Both the specular and the diffuse components of the transmittance and the reflectance were taken into account on each measurement. Infrared transmittance of each Ge wafer was also measured in the IR 2500-25000 nm range (0.5-0.05 eV), using a Nicolet IS10 FTIR spectrometer. Both sets of measurements (UV-

Vis-NIR and IR ranges) were then processed to obtain the final global transmittance in the 300-25000 nm range.

2.5. Simulation

As a way to assess the validity of the measurements, numerical simulations of the transmittance and reflectance parameters along the explored spectral range was performed using the TCAD Silvaco Atlas software, which we also used for the complete modelling of photovoltaic and thermophotovoltaic devices. To this end, a transfer matrix method [26] were used, and optical calculations were performed with the sample structure as in Fig.1 and to fit the experimental EQE of a Ge solar cell in Figure 7.

2.6. EQE measurements

Finally, to extend the usefulness of the obtained complex refraction indices, the EQE of two single-junction Ge solar cells manufactured on the same epiwafer grown by MOVPE was measured in the 600–1800 nm range, and then compared to simulations carried out using the TCAD Silvaco Atlas software. One solar cell was manufactured on the bulk Ge substrate with a thickness of 140 microns while the other cell was chemically thinned till a thickness of 63 microns. EQE measurements were taken using a custom-built system based on a 1000-W Xe-lamp and a triple-grating Horiba Jobin Yvon monochromator (TRIAX180), equipped with a filter wheel and monitor sensors to account for the light source instabilities. The corresponding signal was detected by a eLockIn 203 dual-input 4-phase DSP lock-in amplifier detector in conjunction with an SR570 transconductance preamplifier for each channel.

3. RESULTS AND DISCUSSION

In order to obtain the dielectric function (ε_r, ε_i) for the Ge samples, we must use an optical model which accounts for the sample structure. In this case, it considered three layers, namely, air/Ge-oxide overlayer/semi-infinite Ge substrate (see Figure 1).

The optical constants of the GeO_2 layer were taken from the literature [21]. Its thickness was determined from a fit of the Cauchy function in the optically transparent spectral region below the Ge bandgap (1700-2500 nm), where the extinction coefficient can be assumed as 0. Depending on the germanium sample, thicknesses between 2.7 and 4.9 nm were obtained for the GeO_2 layer. The oxide layer thickness was afterward fixed in a point-by-point fit in the region above the bandgap. Thus, we obtained a set of independent values of pairs of n and k of Ge along the spectra.

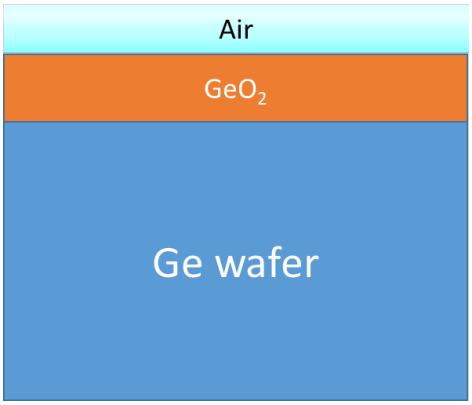

Figure 1: schema of the sample structure optical model used to fit ellipsometry data. Ge wafer is supposed to be semi-infinite, while the GeO_2 layer thickness is obtained after data fitting.

With the aim of obtaining a single dielectric function for each germanium sample along the whole measured spectral range, the multisample analysis of WVASE was used. Under this approach, both ellipsometry data sets (UV-Vis-NIR and IR) are fitted to the same optical model with a dielectric function that covers the entire spectral range studied (UV-Vis-NIR-IR). WVASE software also allows the incorporation of spectrophotometry data (transmittance) into the model fit process. Combining ellipsometry and spectrophotometry data is advantageous since the two techniques are complementary and allow us to obtain complete information about transmitted light. While ellipsometry can accurately measure the thin films' thickness and refractive index, it may have difficulty in accurately measuring the extinction coefficient at very low k values. On the other hand, spectrophotometry can accurately measure the extinction coefficient, but it may not be as sensitive to changes in film thickness or surface roughness as ellipsometry. Therefore, the fitting process included, together, four sets of data corresponding to four different experiments: SE, IRSE, UV-Vis-NIR transmission, and IR transmission.

The WVASE software allows obtaining the sample dielectric function from ~~the~~ linear combination of a set of different types of oscillators, representing the absorption processes of the material in the various spectral regions studied. In our case, we chose a parametric oscillator model to obtain the dielectric function of the Ge samples. The form of the function thus obtained reflects the existence of the characteristic critical points (CP) of the imaginary part of the dielectric function of Ge.

This model consisted of a set of 7 parametric oscillators in the UV-Vis-NIR range, one for each CP previously identified in the literature (E_0, $E_0+\Delta_0$, E_1, $E_1+\Delta_1$, E'_0, E_2, E'_1) [21,22,23,27]. For further information about the mathematical form of these oscillators, the reader is referred to the Supplementary Material file. The direct bandgap transition occurs at the Γ-point in the center of the Brillouin zone, giving rise to both E_0 and $E_0+\Delta_0$ transition due to spin-orbit coupling. Above

the fundamental absorption edge, ε_i rises to an asymmetric peak related to transitions occurring along the eight equivalent <111> directions of the Brillouin zone, E_1. This peak is modelled with an M_1-type parametric semiconductor oscillator. Again, due to the large spin-orbit interaction in the valence band, we can distinguish the E_1 and $E_1+\Delta_1$ transitions. Superimposed on these features, the CP denoted as E'_0 is related to transitions between the valence band and higher conduction bands at the Brillouin zone center. ε_i reaches a strong absolute maximum at E_2 peak, corresponding to contributions from transitions occurring over a large region of the Brillouin zone. This peak has been modelled with an M_2-type parametric semiconductor oscillator. Finally, E'_1 CP has been considered, which can be associated with transitions between the valence bands and higher conduction bands along the <111> directions. Threshold energy, broadening, and amplitude were fitted for each CP. The use of these oscillators ensures the Kramers-Kronig consistency of the functions obtained for ε_r and ε_i. Additionally, for samples with doping levels greater than 10^{16} cm^{-3} (i. e. samples 77944 and 77942), a Drude oscillator was added to take into account the absorption of free-carriers in the NIR and IR regions, which consider both, the frequency at which the electron gas oscillates (plasma frequency ω_p), and the damping constant γ. The Drude oscillator contribution for the real ε_{rD} and imaginary ε_{iD} components of the dielectric function can be expressed, respectively, as

$$\varepsilon_{rD} = \varepsilon_\infty[1 - \omega_P^2/(\omega^2 + \gamma^2)] \quad (1)$$

$$\varepsilon_{iD} = \omega_P^2 \gamma \varepsilon_\infty \left[\frac{\omega}{(\omega^2 + \gamma^2)}\right] \quad (2)$$

where $\omega_P^2 = (4\pi N e^2)/(\varepsilon_0 \varepsilon_\infty m_e^*)$, N is the carrier density, ε_∞ and ε_0 are the dielectric constants of the medium and free space, respectively, and m_e^* is the effective mass of the charge carrier. On the other hand, the damping constant γ is given by $\frac{e}{m_e^* \mu}$ where μ denotes the mobility. In our samples a $m_e^* = 0.28$ was taken [28]. The inclusion of this oscillator is supported by the values obtained from the Hall effect measurements shown in Table 2.

Table 2. Electrical parameters obtained from the Hall effect measurements. Uncertainty is expressed as the standard deviation for a minimum of 10 measurements in each case. For the sake of comparison, nominal values of resistivity and estimated charge carrier concentrations are in italic below the experimental ones.

Sample	Resistivity (Ω cm)	Mobility (cm^2/(Vs))	Charge Carrier Concentration (cm^{-3})	Hall Coefficient (cm^3/C)
77942	(1.856±0.009) × 10^{-2} *0.009-0.03*	731±16	(4.6±0.1) × 10^{17} *10^{18}*	13.6±0.3
77944	(5.90±0.01) × 10^{-2} *0.03-0.07*	1246±3	(8.49±0.02) × 10^{16} *10^{17}*	73.5±0.2
77943	(3.983±0.005) × 10^{-1} *0.2-0.4*	2079±4	(7.54±0.01) × 10^{15} *10^{16}*	828.0±0.5
96132	(21±3) × 10^{0}	-1337±218	(-2.3±0.4) × 10^{14}	-27819±3896

	40		*10^{15}*	

As it may be deduced from the comparison between the values in Tables 1 and 2, the experimental values for resistivity and carrier concentration are in relatively good agreement with the nominal values provided by the samples' manufacturers. However, the experimental concentrations are always below the nominal ones. Besides, the charge sign for the undoped sample (96132) is the opposite of the rest of the samples, which can be explained in terms of an unintentional very small incorporation of n-type dopants or defects during the Ge ingot growth, in the range of 10^{13}-10^{14} which overcompensates the value of the intrinsic carrier concentration (2×10^{13} cm^{-3}).

For the purpose of accounting for the small absorption observed in some other Ge samples in the region below the bandgap (IR region) [19], a series of Gaussian oscillators (up to 3 depending on the sample) was added to the model of parametric oscillators developed for each sample.

Therefore, a Levenberg−Marquardt regression algorithm was used to find the optical model parameters, fitting the SE and transmittance data until a minimum value of the mean-squared error (MSE) was obtained. The goodness of the fits can be confirmed by the comparison between experimental and calculated Stokes parameters after fitting, as it is shown in Figure S1 in the supplementary material file. The resulting fitted dielectric function for each sample is plotted in Figure 2. In the UV-VIS-NIR range, the imaginary part of the dielectric function, ε_i, (Figure 2 bottom left) show rather clearly the different transitions between valence and conduction bands described above (E_0, $E_0+\Delta_0$, E_1, $E_1+\Delta_1$, E'_0, E_2, E'_1). Table 3 gathers the threshold energy and amplitude (between brackets) values of the oscillators associated with each of the seven CPs for the studied sample set obtained after fitting. Additionally, the ratio Δ_0/Δ_1, and MSE values, was included in this table.

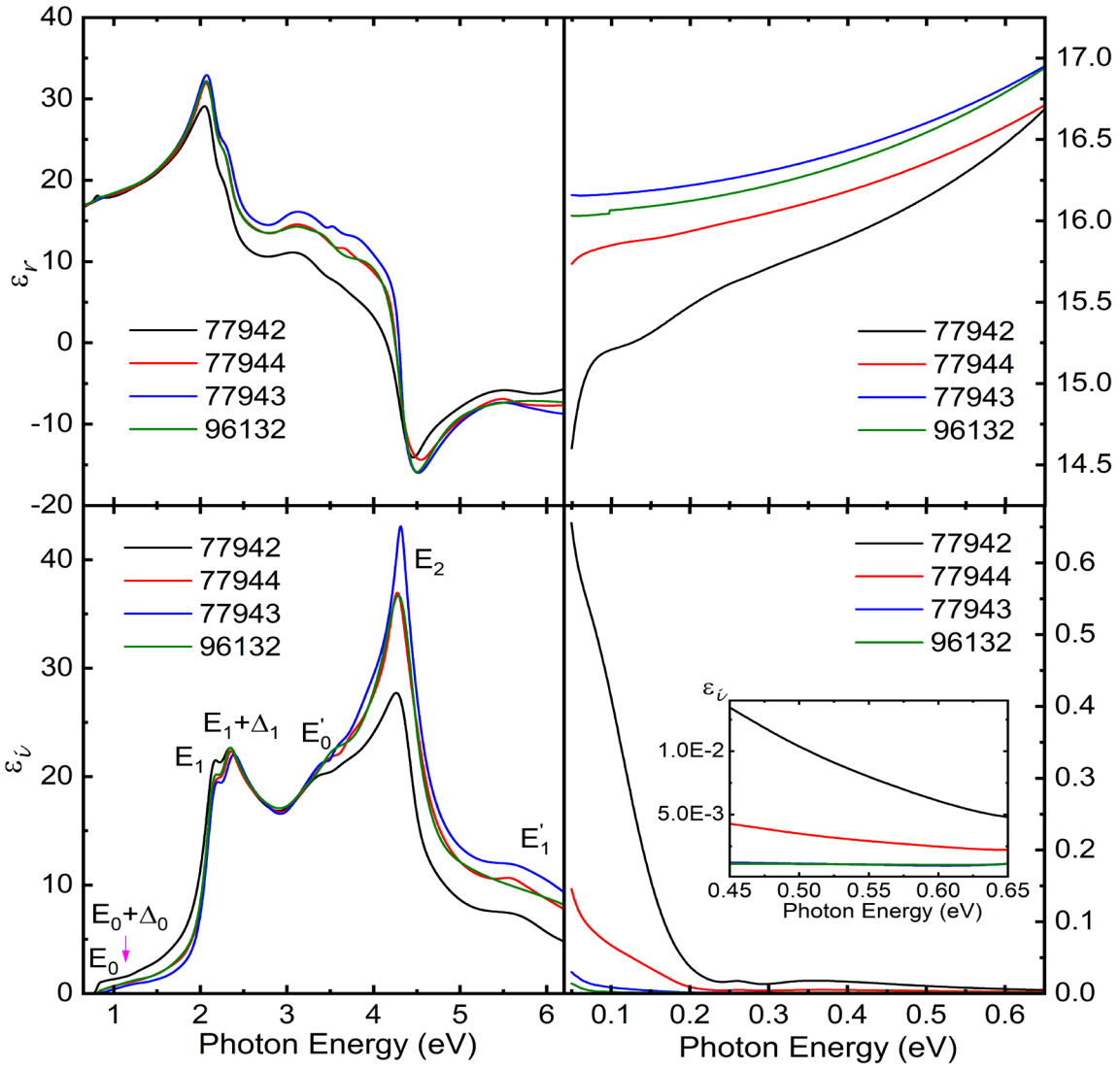

Figure 2: Real (top) and imaginary (bottom), dielectric functions for all the studied samples, including the UV-Vis-NIR (left) and IR (right) ranges. The inset includes details of the imaginary component below the bandgap E_g, demonstrating the low subgap absorption detected from transmission measurements.

Table 3: Values of the threshold energy and amplitude of the oscillators (in parentheses) representing the seven CPs in the UV-Vis-NIR region of the spectrum. Spin-orbit coupling ratio and MSE values have also been included. Samples are ordered from higher (77942) to lower (96132) dopant concentrations.

Sample	E_0 (eV)	$E_0+\Delta_0$ (eV)	E_1 (eV)	$E_1+\Delta_1$ (eV)	E'_0 (eV)	E_2 (eV)	E'_1 (eV)	Δ_0/Δ_1	MSE
77942	0.782 (0.52)	1.050 (0.001)	2.141 (15)	2.310 (18.2)	3.554 (7.7)	4.336 (29)	5.91 (5.5)	1.59	1.03
77944	0.815 (0.25)	1.117 (0.08)	2.122 (16)	2.336 (17)	3.797 (7)	4.273 (38)	5.55 (2.4)	1.41	0.67
77943	0.861 (0.01)	1.140 (0.91)	2.144 (15)	2.306 (15)	3.278 (8)	4.295 (48)	5.66 (8.0)	1.72	0.93
96132	0.831 (0.24)	1.128 (0.62)	2.139 (14)	2.326 (18)	3.620 (9)	4.308 (39)	5.56 (11)	1.59	0.57

For the following analysis, the less doped sample, 96132, was discarded since it was not intentionally doped, and the origin of its dopant concentration estimated from resistivity values and Hall measurements (see Table 2) is thus uncertain (as stated above). For the rest of the samples, the value of E_0 threshold energy decreases when the doping level increases. The observed red shift evidences two competing phenomena [18]. On one hand, due to the filling of the valence (conduction) band with holes (electrons), the Moss-Burstein effect leads to a blue shift in E_0. On the other hand, many-body effects arising from the presence of these free-carriers in the valence or conduction bands (such as, for example, exchange-correlation corrections [29]) reduce the band gap, resulting in a red shift referred to as the "band-gap renormalization" effect. In this case, the second effect prevailed, and this result meets those presented by Xu et al. for n-doped Ge wafers in a very detailed analysis [22 and references therein]. In the same way, for the $E_0+\Delta_0$ transition, the energy values and intensities also decrease when the doping level increases. On the contrary, we do not observe a clear dependence of the E_1 and $E_1+\Delta_1$ transitions parameters with the doping level of the sample, as it was described for some other doped Ge samples [18], though in that work, the doping level was higher than for our samples. Table 3 also includes the values of the ratio Δ_0/Δ_1, and it is observed how the spin-orbit splitting in the valence band along [111], Δ_1, is approximately 2/3 of the spin-orbit splitting at the zone center, Δ_0. Thus, the relationship Δ_0/Δ_1 follows what is known as the 2/3 rule, which provides a consistency check on the identification of the E_1 transitions [30]. Finally, ε_i reaches the absolute maximum in the peak, giving rise to the energy E_2 of this CP. The intensity of this peak is reduced when the doping level increases, in agreement with a previous work [18].

For the analysis of the samples' optical behavior in the IR range, we used the absorption spectra, rather than the sample dielectric functions, in such a way that we can compare our results with previous literature [19]. Absorption, α, can be deduced by a simple calculation from the dielectric function through the following equation

$$\alpha = \frac{2\pi\varepsilon_i}{\lambda(\varepsilon_r)^{1/2}} \qquad (3)$$

In Figure 3, we have represented this parameter for our samples as a function of photon energy and wavelength. We can distinguish five different processes from the highest to the lowest energy (right to left in the figure). Transitions corresponding to the direct bandgap (0.75-0.85 eV), which are assigned to the CP E_0 and are associated with carrier transitions, assisted only by photons, from the highest energy state of the valence band to the lowest energy state of the conduction band. The nominally undoped sample (96132, red line in figure 3) do not follow the general trend observed for the rest of the samples, but we must remember the n-type doping found after Hall effect measurements for this sample, while the rest of the samples are p-type doped. On the left side of the direct gap transition, we can see the one corresponding to the indirect bandgap, where carrier transitions occur from the valence band to the conduction band in two steps, one that includes a photon-electron interaction and another one including a

phonon-electron interaction (see figure 4 for a more detailed description of this transition). At energies below the indirect bandgap, absorption due to the ordinary conduction effect of free carriers occur (free-carrier absorption, FCA). In p-type semiconductors, they can be explained on the basis of the Drude model, which, unlike for metals, present a dependence on the carrier concentration. In these processes, the initial and final states of the electron are in the same band, so these processes are called *intraband processes*. Besides, free-carrier *interband absorption* processes can also occur at lower energy values. These processes cannot be explained in terms of the Drude theory, and they are associated with intervalence band transitions. These absorption bands are marked in the figure as (3) at 0.40 eV, (2) at 0.26 eV, and (1) at 0.15 eV, and they are clearly visible for the two more doped samples. They can be assigned to the spin-orbit split to a heavy hole band, to the spin-orbit split to light hole band, and to the light hole band to heavy hole band transitions, respectively [19]. Finally, at the lowest energy values, absorptions derived from lattice vibrations (optical phonons) are observed.

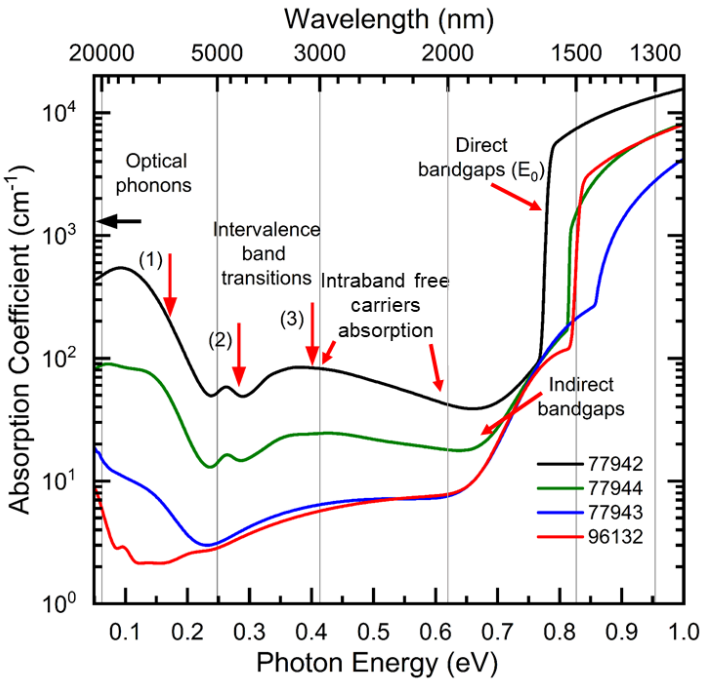

Figure 3: Absorption spectra obtained for the studied samples. Vertical grey lines are a guide to the eye. From right to the left, red arrows mark the region for the direct bandgaps (between 0.75 and 0.85 eV), indirect bandgaps (around 0.65 eV), the approximate energy region where FCA processes occur, and the 3 intervalence band transitions.

Using these absorption spectra in a restricted spectral range, the determination of the indirect bandgap was performed by the Tauc method. The Tauc method, also known as the Tauc plot, is a widely used technique to determine the optical bandgap of semiconductors or other materials with a direct or indirect bandgap. In the Tauc method, the absorption coefficient (α) is plotted as

a function of the photon energy ($h\nu$), where h is Planck's constant and ν is the frequency of the incident light. The absorption coefficient is related to the material's bandgap, E_g, through the following equation

$$\alpha(h\nu) = A(h\nu - E_g)^m \quad (4)$$

where A is a constant related to the material's transition matrix elements, and m is an exponent that depends on the type of electronic transition. In this case, for an indirect allowed transition, one must plot $(\alpha h\nu)^{1/m}$, with $m = 2$, as a function of photon energy $(h\nu)$. The Tauc plots for all the investigated samples, considering the indirect bandgap representation in Figure 4, show a linear region at higher photon energies than the bandgap, corresponding to the onset of significant absorption. The extrapolation of this linear region to the x-axis (α = 0) gives an estimate of the indirect bandgap energy. The values obtained for the indirect bandgap fall within the range of 0.62-0.66 eV and are ordered according to the charge carrier density values obtained in Hall effect measurements, the higher the dopant concentration, the smaller the bandgap (see inset in Figure 4).

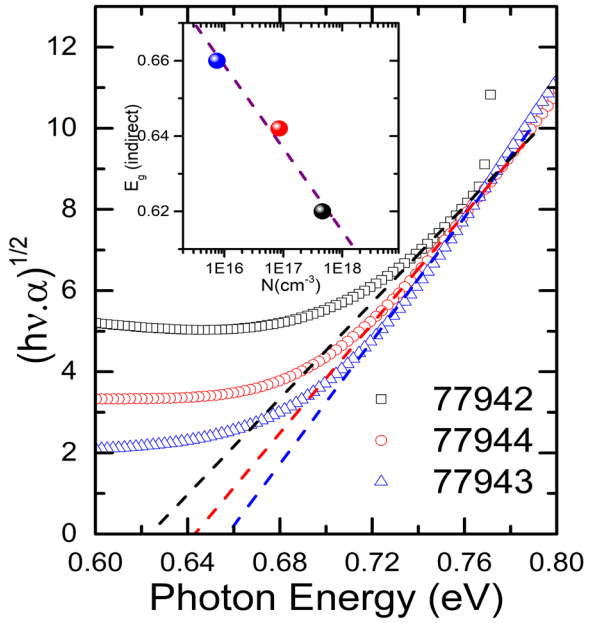

Figure 4: Determination of the indirect bandgap using the Tauc method. Only the intentionally doped samples have been included in this figure. Inset: values of the charge carrier density obtained from Hall effect measurements.

Finally, from the dielectric function, the complex refraction index of these wafers was obtained. They are represented in Figure 5, together with those deduced from [20] in the UV-Vis-NIR range, and [19] in the IR spectrum, for similar doping levels. For the sake of clarity, figures were represented in two separated spectral ranges, UV-Vis-NIR on the left panels and IR on the right panels. For the first spectral range, we can notice very small differences. In the IR range,

differences are much more noticeable, though reader must pay attention to the different Y-axis scale between figures on the left and on the right. The most remarkable feature is the higher extinction coefficient as compared with that deduced from [19,20] for all the dopant concentrations.

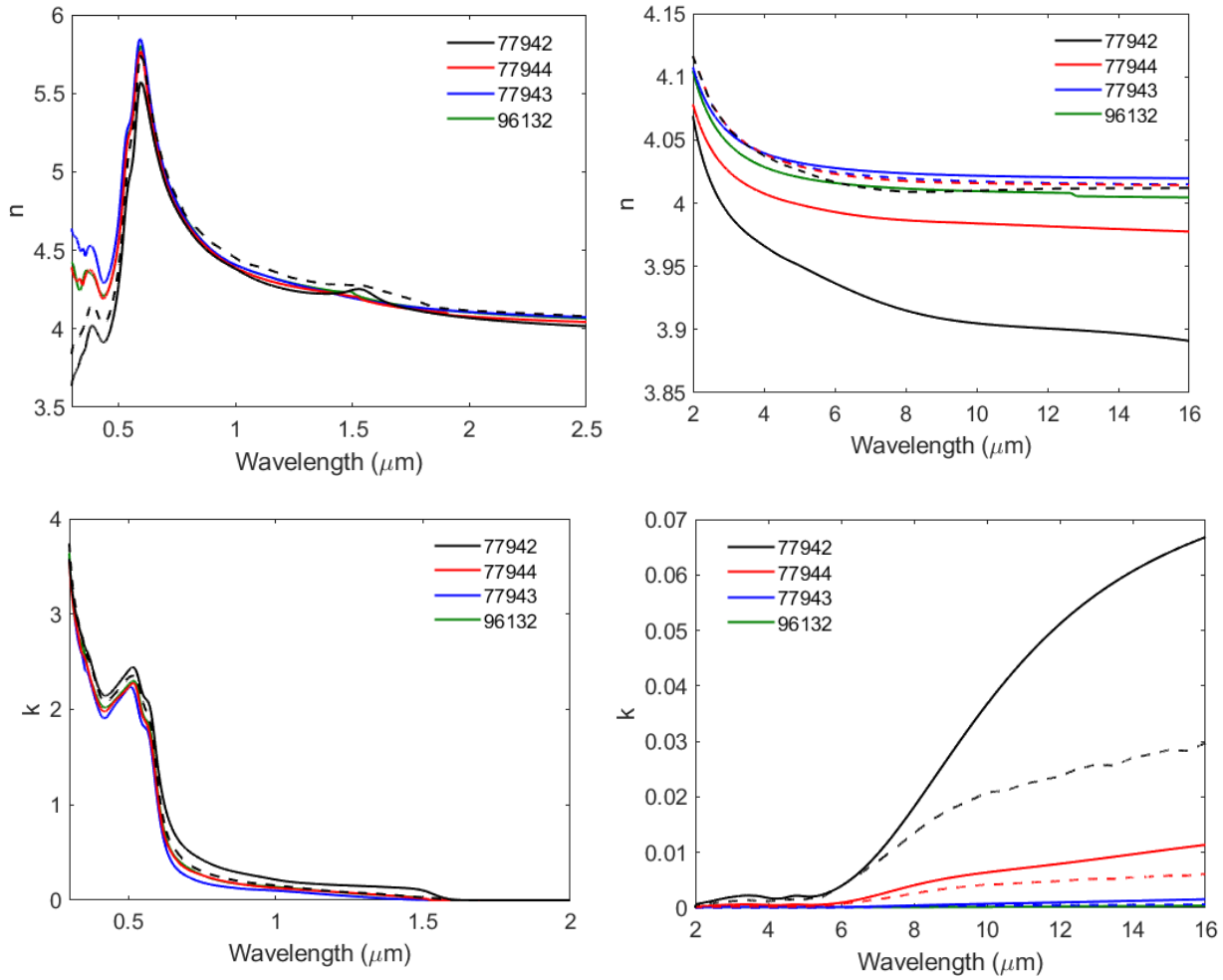

Figure 5: Complex refraction indices (refractive index, n, upper panels, extinction coefficient, k, lower panels) obtained from the dielectric functions of the samples (solid lines), compared with those deduced from [20], left, and [19], right, for similar doping levels than our samples nominal dopant concentrations (dashed lines). Figures on the left correspond to UV-Vis-NIR spectral range while figures on the right account for the IR spectral range. Dashed lines lie on the solid lines for most of the UV-Vis-NIR spectrum.

As a means to further ensure the validity of the obtained complex refraction indices shown in Figure 5, both reflectance and transmittance for all the samples were simulated using the Silvaco Atlas software, using as input the refraction indices shown in Figure 5. Optical calculations were performed using the transfer matrix method [26]. The simulated and experimental reflectance and transmittance were compared along the measured spectral range, and they are shown in Figure 6. Reflectance simulations show the same behaviour as experimental data in all the measured range, although a slight offset is observed between them. Similarly, transmittance

obtained from simulation results (solid lines) is almost identical to the experimental data (symbols) for the two samples with higher doping concentrations along the whole spectral range. For the other two samples (i.e., 96132, 77943) a slight deviation is observed in the infrared range. However, this offset is within the range of uncertainty of the experimental measurements. As shown in detail in Figure S2 in the supplementary material file, these offsets are always smaller than 3% for reflectance and 2% for transmittance along the respective spectral ranges. Thus, it can be said that the simulation model is able to reproduce both the experimental transmittance and reflectance of the four samples, validating our results.

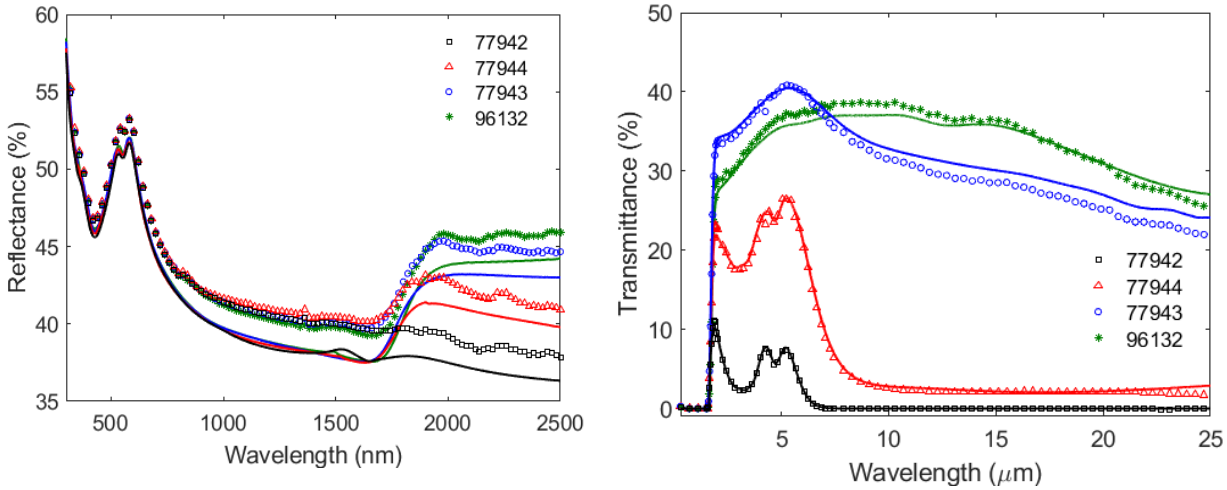

Figure 6. Measured (colored hollow symbols) and simulated (solid lines) reflectance (left) and transmittance (right) of the Ge wafers, respectively. Note the different X-axis scales between both figures.

An additional validation of the complex refraction indices obtained in this work was accomplished. We fabricated by MOVPE a single-junction germanium solar cell epiwafer onto a commercial Ge substrate with a nominal p-type concentration of 3×10^{17} cm^{-3} which is in between the two more doped wafers of this paper. Two different solar cells were manufactured on the same epiwafer (see the solar cell structure in Figure 7 top left), namely, a non-thinned cell by using the bulk Ge substrate with a thickness of 140 microns, and a thinned cell by etching the Ge substrate up to 63 microns through an in-house developed formulation [31]. The complex refraction indices corresponding to the doping level of these solar cells were interpolated from those obtained for the samples presented in Figure 5. Since the extinction coefficient, k, accounts for both, the effective absorption (which produces photogeneration), but also to the free-carrier absorption (which does not produce photogeneration), we have obtained an effective extinction coefficient, where the FCA contribution was discarded (see the Supplementary Material file for more information), by fitting the EQE of the non-thinned solar cell. The comparison between the extinction factor as deduced from those obtained in this work according to the dopant level of the Ge wafer, and the effective k without the FCA contribution is shown in Figure 7 top right. Afterwards, the resulting complex refraction indices were introduced as an input for the simulation of the EQE of the Ge solar cells using the Silvaco Atlas software. The experimental and simulated EQEs of both cells are shown in lower panels of Figure 7. The spectral range was

restricted to the wavelengths of interest when the Ge cell is incorporated as the bottom subcell to a MJSC. The comparison between both, the measured (blue hollow circles in Figures 7 bottom left and right), and simulated (blue solid lines in Figures 7 bottom left and right) EQE, for both, thinned and non-thinned cells, match along the whole spectral range, which is a proof of the goodness of the complex refraction indices interpolated from those determined for our samples. Besides, simulated EQEs for both solar cells obtained by using the complex refraction indices deduced from [20] are also included in lower panels of Figure 7 (red solid lines). In this case, there are noticeable differences with the measured EQE in the high wavelength regime. It can be argued that because the EQE fitting is multiparametric, red lines could better match the experimental EQE if different solar cell parameters were used. We have tried a better fitting using the complex refraction index in [20] by modifying the electron lifetime in the base of the cell, and the back surface recombination velocity, but we never got a perfect match with experimental measurements, thus suggesting that the good fitting is related with the optical parameters. These simulations carried out on real solar cells provide additional confidence on the complex refraction indices as determined in this work. Therefore, our complex refraction indices have demonstrated their suitability to describe the optical behavior of the studied Ge wafers and, besides, they allow the prediction of a Ge solar cell performance as a function of the Ge wafer doping level and the solar cell thickness.

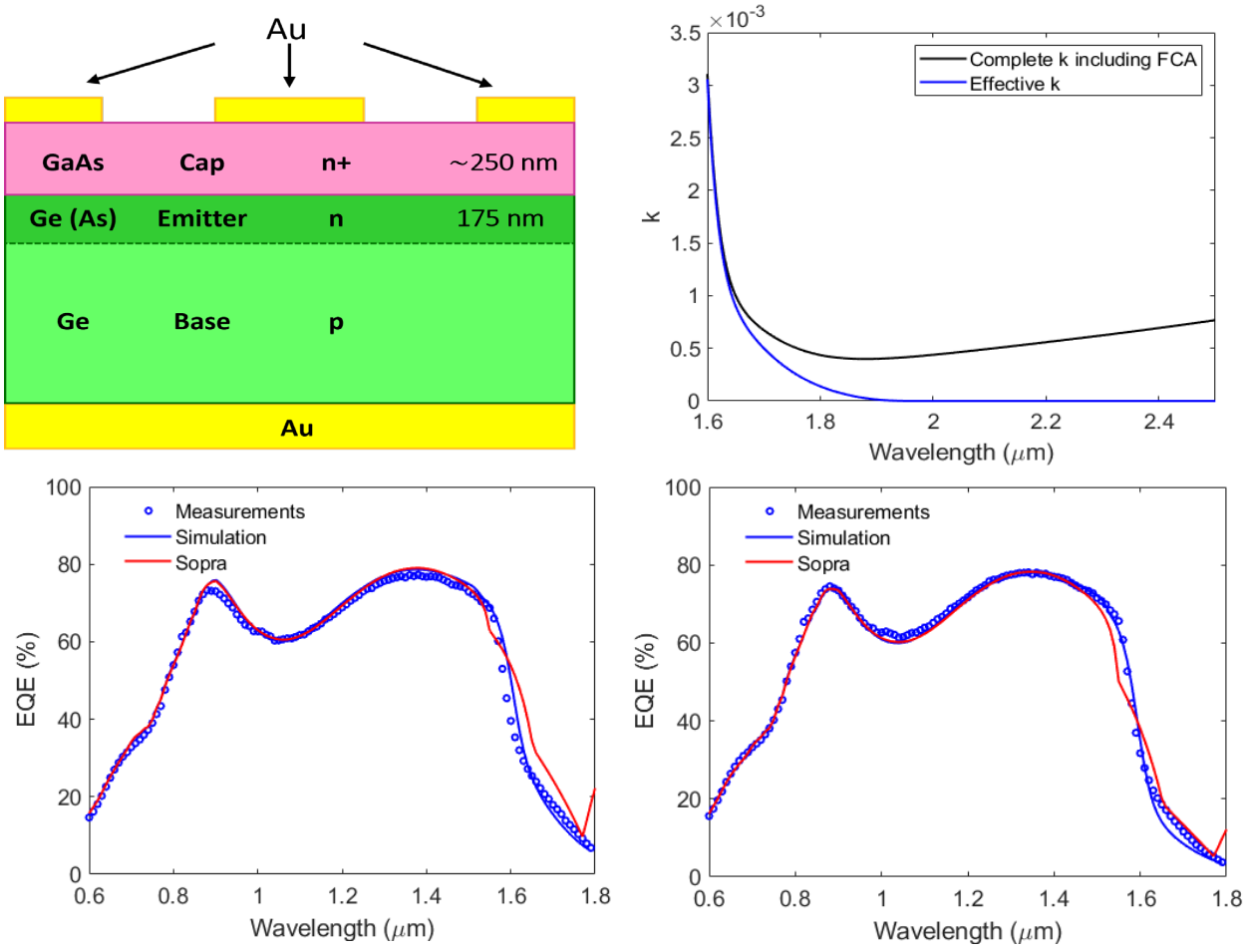

Figure 7: Upper panels, left, structure of a single-junction Ge solar cell whose experimental EQE (for the typical spectral range of interest for a bottom cell in a MJSC) is measured; right, values of the extinction coefficient as derived from this study, including FCA (black line) and the effective one required for the EQE simulation (blue line). Lower panels, experimental and simulated EQE of the non-thinned solar cell (140 microns, left), of the thinned solar cell (63 microns, right). Complex refraction index used to depict the blue solid line are those calculated in this work, while the red line was simulated using complex refraction index as deduced from [20].

4. CONCLUSIONS

This work intends to achieve the refractive-indices of Ge p-type substrates as a function of doping level for a non-existing wavelength range (200 to 25000 nm) which can be used in the modelling and simulation of photovoltaic and thermophotovoltaic devices. The dielectric functions of four commercial Ge wafers have been determined through the analysis of spectroscopy ellipsometry measurements combined with transmittance measurements. Dopant concentration (nominally $10^{15} – 10^{18}$ cm^{-3}) was different in each wafer, in such a way, the dielectric functions were obtained as a function of doping. The experimental data were fitted to a linear combination of oscillators that ensures the Kramers-Kroning consistency of our model.

The complex refraction indices of the Ge wafers were calculated subsequent to the dielectric functions. They are quite similar to former refraction indices for similar dopant levels along UV-Vis-NIR range. However, in the IR range, differences due to dopant concentration are more evident in our complex refraction indices.

These complex refraction indices enable the simulation and comparison of the reflectance and transmittance of each wafer to measured values. Notably, there is a strong correlation between the simulated and experimental data across the entire spectral range (0.2 to 25 microns). The estimated differences are less than 3% for reflectance, and 2% for transmittance, thereby proving the effectiveness of the calculated refractive indices in describing the optical behavior of these Ge wafers.

As further validation, two Ge single-junction solar cells were manufactured by MOVPE, namely one with a thickness of 140 microns and the other one with a thinned thickness of 63 microns on a Ge wafer with a different dopant concentration than those measured in this study. For these two solar cells, we have determined their refractive indices, and effective extinction coefficients, from the (n, k) values obtained for the Ge wafers measured in this work. Both, n and effective k, were used as an input to simulate the EQE of these two solar cells. The comparison between the simulated and experimentally measured EQE, revealed a very good match (better than the obtained using complex refraction indices from the literature) across the spectral range of interest (600 to 1800 nm), which underscores the aptness of our findings for determining the complex refraction index of a Ge wafer as a function of doping.

These results mark a significant improvement over previous studies since our complex refraction indices cover an ample wavelength range, from 0.2 to 25 microns, which constitute an advance over prior published results. This fact will extend their applicability for a wide variety of

optoelectronic devices. In particular, they will have a crucial role in the modelling and simulation of Ge based devices such in flexible and lightweight III-V multijunction solar cells and also for Ge thermophotovoltaic converters.

Acknowledgments

This work has been partially supported by the Grant PID2020-112763RB-I00 funded by Ministerio de Ciencia e Innovación (MCIN/AEI/10.13039/501100011033). The epitaxy runs reported in this paper were carried out in a MOVPE reactor retrofitted with project RENOAIX200 (grant number EQC2019-005701-P) funded also by Spanish MCIN/AEI (AEI/10.13039/501100011033) and FEDER funds "Una manera de hacer Europa". Spectroscopy ellipsometry measurements were funded by Ministerio de Ciencia e Innovación under the project reference EQC2019-005503-P. Part of the equipment used in this research for solar cell manufacturing was acquired through project LABCELL30 [grant number EQC2021-006851-P] with funding from the Spanish Ministerio de Ciencia e Innovación /Agencia Estatal de Investigación [MCIN/AEI 10.13039/501100011033] and the European Union "Next Generation EU"/PRTR", European Regional Development Fund (ERDF) “A way to make Europe” and by the Universidad Politécnica de Madrid through “Ayudas para la cofinanciación de infraestructuras de I+D+I (Programa Propio)”.

References

[1] D.C. Law, X.Q. Liu, J.C. Boisvert, E.M. Redher, C.M. Fetzer, S. Mesropian, R.R. King, K.M. Edmondson, B. Ju, R.L. Woo, D.D. Krut, P.T. Chiu, D.M. Bhusari, S.K. Sharma, N.H. Karam, Recent progress of Spectrolab high-efficiency space solar cells, Conference record of the IEEE Photovoltaic Specialist Conference (2012) 3146-3149. https://doi.org/ 10.1109/PVSC.2012.6318246.

[2] J. Baker, C.P. Allford, S. Gillgrass, T. Peach, A.D. Johnson, A.M. Joel, S.W. Lim, M. Geen, J.I. Davies, S. Shutts, P.M. Smowton, Comparative study of 940 nm VCSELs grown on Ge and GaAs substrates, 2022 IEEE Photonics Conference (IPC), Vancouver, BC, Canada (2022). https://doi.org/10.1109/IPC53466.2022.9975478.

[3] C.D. Mendoza, P.G. Caldas, F.L. Jr. Freire, M.E.H. Maia da Costa, Growth of single-layer Graphene on Ge (100) by chemical vapor deposition, Appl. Surf. Sci. 447 (2018) 816 – 821. https://doi.org/10.1016/j.apsusc.2018.04.019.

[4] J. Sitek, I. Pasternak, J. Grzonka, J. Sobieski, J. Judek, P. Dabrowski, M. Zdrojek, W. Strupinski, Impact of germanium substrate orientation on morphological and structural properties of graphene grown by CVD method, Appl. Surf. Sci. 499 (2020) 143913. https://doi.org/ 10.1016/j.apsusc.2019.143913.

[5] Y. Zhao, D. Han, X. Wang, Z. Hu, Y. Chen, Y. Chen, D. Zhou, Y. Li, E.G. Fu, Z. Zhao, A facile approach to direct growth of layer-tunable graphene on Ge substrate, Carbon 153 (2019) 776-782. https://doi.org/10.1016/j.carbon.2019.07.029.

[6] L.L. McDowell, M.R. Mirzaei, B. Weng, Z. Shi, Integration of epitaxial IV-VI Pb-chalcogenide on group IV vicinal Ge substrate to form p-n heterogeneous structures, Cryst. Growth & Design 22 (2022) 461-468. https://doi.org/ 10.1021/acs.cgd.1c01074.

[7] S. Wirths, D. Buca, S. Mantl, Si-Ge-Sn alloys: from growth to applications, Prog. Cryst. Growth & Charact. Mater. 62 (2016) 1-39. https://doi.org/10.1016/ j.pcrysgrow.2015.11.001.

[8] G. Timò, G. Abagnale, N. Armani, M. Calicchio, B. Schineller, MOVPE SiGeSn development for the next generation four junction solar cells, AIP Conference Proceedings 2012 (2018) 040011. https://doi.org/10.1063/1.5053519.

[9] S.J. Gillgrass, C.P. Allford, T. Peach, J. Baker, A.D. Johnson, J.I. Davies, A.M. Joel, S. Shutts, P.M. Smowton, Impact of thermal oxidation uniformity on 150 mm GaAs- and Ge-substrate VCSELs, J. Phys. D: Appl. Phys. 56 (2023) 154002. https://doi.org/10.1088/1361-6463/acc040.

[10] E. Winter, W. Schreiber, P. Schygulla, P.L. Souza, S. Janz, D. Lackner, J. Ohlmann, III-V material growth on electrochemically porosified Ge substrates, J. Cryst. Growth 602 (2023) 126980. https://doi.org/10.1016/j.jcrysgro.2022.126980.

[11] I. Rey-Stolle, E. Barrigón, B. Galiana, C. Algora, Analysis of germanium epiready wafers for III–V heteroepitaxy. J. Cryst. Growth 310 (2008) 4803-4807. https://doi.org/10.1016/j.jcrysgro.2008.07.116.

[12] M. Gabás, S. Palanco, S. Bijani, E. Barrigón, C. Algora, I. Rey-Stolle, I. García, J.R. Ramos-Barrado, Analysis of the surface state of epi-ready Ge wafers, Appl. Surf. Sci. 258 (2012) 8166-8170. https://doi.org/ 10.1016/j.apsusc.2012.05.015.

[13] L. Barrutia, I. García, E. Barrigón, M. Ochoa, I. Lombardero, M. Hinojosa, P. Cano, J. Bautista, L. Cifuentes, I. Rey-Stolle, C. Algora, Development of the lattice matched GaInP/GaInAs/Ge triple junction solar cell with an efficiency over 40%, 2018 Spanish Conference on Electron Devices (CDE), Salamanca, Spain, 2018, 1-4. https://doi.org/10.1109/CDE.2018.8596996.

[14] H.B. Briggs, R.C. Fletcher, New infrared absorption bands in p-type germanium, Phys. Rev. 87 (1952) 1130-1131. https://doi.org/10.1103/PhysRev.87.1130.
[15] H.B. Briggs, R.C. Fletcher, Absorption of infrared light by free-carriers in germanium, Phys. Rev. 91 (1953) 1342-1346. https://doi.org/10.1103/PhysRev.91.1342.
[16] S. Munusue, T. Arai, The intrinsic absorption edge of heavily doped n- and p-type germanium, Jpn. J. Appl. Phys. 3 (1964) 269-275. https://doi.org/10.1143/JJAP.3.269.
[17] Om P. Rustgi, J. S. Nodvik, G. L. Weissler, Optical constants of germanium in the region 0-27 eV, Phys. Rev. 122 (1961) 1131-1134. https://doi.org/10.1103/PhysRev.122.1131.
[18] L. Viña, M. Cardona, Optical properties of pure and ultraheavily doped germanium: Theory and experiment, Phys. Rev. B 34 (1986) 2586-2597. https://doi.org/10.1103/PhysRevB.34.2586.
[19] M. Nedeljkovic, R. Soref, G.Z. Mashanovich, Predictions of free-carrier electroabsorption and eletrorefraction in germanium, IEEE Photonics J. 7 (2015) 2600214. https://doi.org/10.1109/JPHOT:2015.2419217.
[20] http://www.sspectra.com/sopra.html
[21] T.N. Nunley, N.S. Fernando, N. Samarasingha, J.M. Moya, C.M. Nelson, A.A. Medina, S. Zollner, Optical constants of germanium and thermally grown germanium dioxide from 0.5 to 6.6 eV via a multisample ellipsometry investigation, J. Vac. Sci. Technol. B 34 (2016) 061205. https://doi.org/10.1116/1.4963075.
[22] C. Xu, J. Kouvetatis, J. Menéndez, Doping dependence of the optical dielectric function in n-type germanium, J. Appl. Phys. 125 (2019) 085704. https://doi.org/10.1063/1.5084277.
[23] C. Emminger, F. Abadizaman, N.S. Samarasingha, T.E. Tiwald, S. Zollner, Temperature dependent dielectric function and direct bandgap of Ge, J. Vac. Sci. Technol. B 38 (2020) 012202. https://doi.org/10.1116/1.5129685.
[24] P. Martín, V. Orejuela, C. Sanchez-Perez, I. García, I. Rey-Stolle, "Device Architectures for Germanium TPV Cells with Efficiencies over 30%", CDE-14 Conference Proceedings in IEEE Xplore (in press), 2023.
[25] I. Lombardero, L. Cifuentes, M. Gabás, C. Algora, Manufacturing process for III–V multijunction solar cells on germanium substrates with a total thickness below 60 microns, Prog. Photovolt. Res. Appl. 30 (2022) 740-749. https://doi.org/10.1002/pip.3547.
[26] E. Centurioni, Generalized matrix method for calculation of internal light energy flux in mixed coherent and incoherent multilayers, Appl Opt. 44 (2005) 7532-7539. https://doi.org/10.1364/ao.44.007532.
[27] M. Cardona, Modulation Spectroscopy, Solid State Physics, Suppl. 11, (Academic, New York 1969) 55-65
[28] R.N. Dexter, H.J. Zeiger, B. Lax, Cyclotron resonance experiments in silicon and Germanium. Phys. Rev. 104 (1956), 637–644. https://doi.org/10.1103/PhysRev.104.637.
[29] S. Das Sarma, R. Jalabert, S.R. Eric Yang, Band-gap renormalization in semiconductor quantum wells, Phys. Rev. B 41 (1990), 8288-8294. DOI: 10.1103/PhysRevB.41.8288.
[30] P.Y. Yu, M. Cardona, Fundamentals of Semiconductors, 4th ed. Springer
[31] C. Sanchez-Perez, I. García, I. Rey-Stolle, Fast chemical thinning of germanium wafers for optoelectronic applications, App. Surf. Sci. 579 (2022), 152199. https://doi.org/10.1016/j.apsusc.2021.152199.